JACS
JOURNAL OF THE AMERICAN CHEMICAL SOCIETY
Article
pubs.acs.org/JACS

Intricate Short-Range Ordering and Strongly Anisotropic Transport Properties of $Li_{1-x}Sn_{2+x}As_2$

Kathleen Lee,[†] Derrick Kaseman,[‡] Sabyasachi Sen,[‡] Ivan Hung,[§] Zhehong Gan,[§] Birgit Gerke,[⊥] Rainer Pöttgen,[⊥] Mikhail Feygenson,[∥] Jörg Neuefeind,[∥] Oleg I. Lebedev,[#] and Kirill Kovnir*[,†]

[†]Department of Chemistry and [‡]Department of Chemical Engineering and Materials Science, University of California—Davis, One Shields Avenue, Davis, California 95616, United States

[§]Center of Interdisciplinary Magnetic Resonance, National High Magnetic Field Laboratory, 1800 East Paul Dirac Drive, Tallahassee, Florida 32310, United States

[⊥]Institut für Anorganische und Analytische Chemie, Universit ät Münster, Corrensstrasse 30, 48149 Münster, Germany

[∥]Chemical and Engineering Materials Division, Oak Ridge National Laboratory, Oak Ridge, Tennessee 37831, United States

[#]Laboratoire CRISMAT, UMR 6508, ENSICAEN-CNRS, Université Caen, 14050 Caen, France

Supporting Information

ABSTRACT: A new ternary compound, $Li_{1-x}Sn_{2+x}As_2$, $0.2 < x < 0.4$, was synthesized via solid-state reaction of elements. The compound crystallizes in a layered structure in the $R\bar{3}m$ space group (No. 166) with Sn−As layers separated by layers of jointly occupied Li/Sn atoms. The Sn−As layers are comprised of Sn_3As_3 puckered hexagons in a chair conformation that share all edges. Li/Sn atoms in the interlayer space are surrounded by a regular As_6 octahedron. Thorough investigation by synchrotron X-ray and neutron powder diffraction indicate no long-range Li/Sn ordering. In contrast, the local Li/Sn ordering was revealed by synergistic investigations via solid-state ^{6,7}Li NMR spectroscopy, HRTEM, STEM, and neutron and X-ray pair distribution function analyses. Due to their different chemical natures, Li and Sn atoms tend to segregate into Li-rich and Sn-rich regions, creating substantial inhomogeneity on the nanoscale. The inhomogeneous local structure has a high impact on the physical properties of the synthesized compounds: the local Li/Sn ordering and multiple nanoscale interfaces result in unexpectedly low thermal conductivity and highly anisotropic resistivity in $Li_{1-x}Sn_{2+x}As_2$.

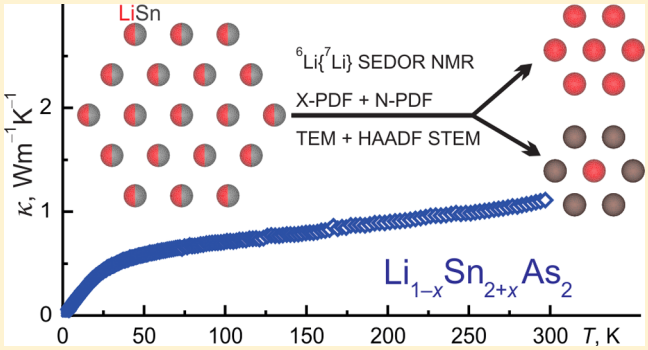

INTRODUCTION

The crystal structures of materials define their properties, and these properties crucially depend on local structural features, such as disorder or defects. Detailed characterization of such structural features is challenging, especially if light elements like lithium are involved. Lithium-ion battery electrodes and solid electrolytes are examples of partially disordered Li solids where knowledge of the atomic positions of Li and the diffusion pathways is important for designing materials with superior characteristics.[1−3] Significant progress was recently achieved in characterizing the lithiation products of elemental electrodes, e.g., Li−Si or Li−Sn.[4−6] However, little is known about many binary compounds' abilities to react with or intercalate Li, and the structures and properties of Li-containing ternary phases remain unexplored.[7,8]

Short- and long-range inhomogeneities play an important role in the design of thermoelectric materials. For example, in Zn_4Sb_3, the zinc atoms, which are distributed over several atomic positions and located in interstitial sites, significantly lower the thermal conductivity of the material, resulting in a high thermoelectric figure of merit.[9−12] $Ba_8Au_{16}P_{30}$ was found to have one of the lowest lattice thermal conductivities among solid crystalline compounds.[13] The low lattice thermal conductivity was attributed to the presence of twinning and antiphase boundaries in the material, despite it being fully ordered on the atomic scale. Compounds with joint site occupation between heavy and light atoms can also reduce the thermal conductivity of materials. Recently, Li cations were successfully used in thermoelectric materials where traditionally heavy elements are applied to achieve low thermal conductivity.[14] The Kanatzidis group studied compounds with joint site occupation between heavy (Pb, Sb) and light atoms (Li) to scatter heat-carrying phonons and reduce the lattice thermal conductivity.[14] In $LiPbSb_3S_6$, an extremely low thermal conductivity of 0.24 W m^{-1} K^{-1} at room temperature was achieved. Our interest in new ways of reducing thermal conductivity prompted our systematic search for new ternary

Received: January 8, 2015
Published: February 22, 2015

DOI: 10.1021/jacs.5b00237
J. Am. Chem. Soc. 2015, 137, 3622−3630

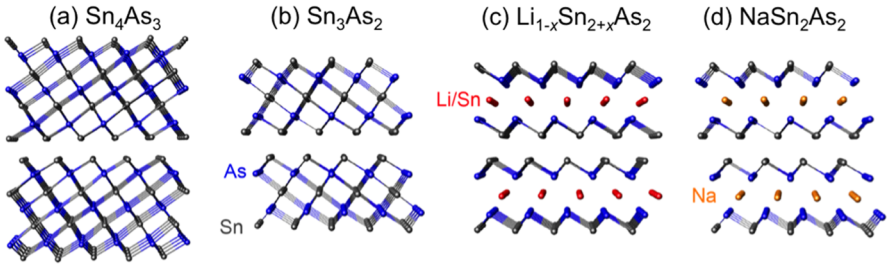

Figure 1. Crystal structures of (a) Sn_4As_3; (b) a hypothetical binary compound Sn_3As_2; (c) the title compound $Li_{1-x}Sn_{2+x}As_2$; and (d) $NaSn_2As_2$. Color code: gray, Sn; blue, As; red, Li/Sn; orange, Na.

tetrelide-pnictides. Here we report the synthesis, crystal structure, and complicated local ordering pattern for $Li_{1-x}Sn_{2+x}As_2$. Determination of the exact structure of partially ordered materials containing Li atoms requires going beyond conventional characterization methods. We applied a combination of high-resolution synchrotron powder X-ray diffraction, solid-state SEDOR NMR spectroscopy, electron diffraction (ED), high-resolution transmission electron microscopy (HRTEM), high-angle annular dark-field scanning transmission electron microscopy (HAADF-STEM), and X-ray and neutron pair distribution function analyses to determine the local ordering on the atomic and nanoscale. Local ordering greatly impacts the thermal and electron transport properties in the investigated materials.

EXPERIMENTAL SECTION

Single-phase samples of $Li_{1-x}Sn_{2+x}As_2$ were prepared via solid-state reactions. All materials were handled in an argon-filled glovebox ($p(O_2) \leq 1$ ppm). The starting materials, tin shot (Alfa Aesar, 99.7%) and arsenic (Alfa Aesar, 99.9999%), were used as received. The surface layer of the metallic lithium granules (Alfa Aesar, 99%) was scraped off before use. Single-phase samples of the composition $Li_{0.7}Sn_{2.3}As_2$ were synthesized by combining the elements in a molar ratio of 0.7 Li: 2.3 Sn:2 As with a 5 mg excess of Li and a total weight of 200 mg. The elements were sealed inside an evacuated and carbonized silica ampule. The ampule was heated to 973 K over 10 h, annealed for 2 h, and subsequently cooled to 423 K over 30 h. Other compositions were synthesized in a similar manner with stoichiometric amounts of Sn and As and a 5 mg excess of Li. The reaction products were single silver-colored ingots, which broke into large plate-like crystals approximately $0.5 \times 0.5 \times 0.2$ mm in size. The products were stable upon heating in air to 423 K and resistant to oxidation at room temperature for several months, though they slowly decomposed into binary tin arsenides. Synthesized samples were stored in an Ar-filled glovebox.

$Li_{1-x}Sn_{2+x}As_2$ was characterized by single-crystal X-ray diffraction, high-resolution and laboratory powder X-ray diffraction (XRD), X-ray and neutron pair distribution function (PDF) analyses, differential scanning calorimetry (DSC), ^{119}Sn Mössbauer spectroscopy, solid-state ^{7}Li and ^{6}Li nuclear magnetic resonance (NMR) spectroscopy, energy-dispersive X-ray spectroscopy (EDXS), high-resolution transmission electron microscopy (HRTEM), high-angle annular dark-field scanning transmission electron microscopy (HAADF-STEM), quantum chemical calculations, and magnetic and transport properties measurements. Experimental details are provided in the Supporting Information (SI).

RESULTS AND DISCUSSION

Synthesis. The compound was initially synthesized from a reaction of elements with the molar ratio 1:4:3 for Li:Sn:As that were annealed at 873 K for 96 h. Single-crystal X-ray diffraction was performed on a crystal, and structure refinement gave the composition $Li_{0.692(2)}Sn_{2.308}As_2$. Further reactions were carried out varying the Li content and using the annealing profile described in the Experimental Section. This profile was optimized using the reported synthetic conditions for $NaSn_2As_2$.[15] During annealing, Li reacted with the carbon layer and the silica ampule causing the black carbon layer to turn blue. An excess of 5 mg of Li was used to compensate for the reaction with the ampule. The compound formed during slow cooling; faster cooling rates or quenching from high temperatures produced admixtures of Sn_4As_3 and SnAs. Slow cooling may promote phase separation of $Li_{1-x}Sn_{2+x}As_2$ into large grains of Sn_4As_3.

Crystal Structure. The crystal structure of $Li_{1-x}Sn_{2+x}As_2$ can be described as a derivative of a binary tin arsenide, Sn_4As_3 (Figure 1a). Sn_4As_3 has alternating layers of tin and arsenic atoms that are combined into Sn-terminated seven-layer blocks that stack along the *c*-axis. Within the block, a layer of arsenic atoms separates each layer of tin atoms. Removing two layers within the seven-layer block would result in the hypothetical binary compound Sn_3As_2 (Figure 1b). From the hypothetical binary compound Sn_3As_2, partial substitution of the tin atoms in the central layer would result in the crystal structure of $Li_{1-x}Sn_{2+x}As_2$ (Figures 1c and 2). The crystal structure of $Li_{1-x}Sn_{2+x}As_2$ is also similar to the Na analogue, $NaSn_2As_2$

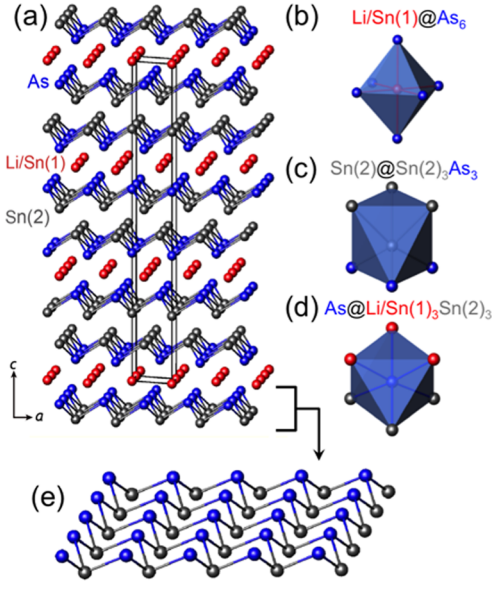

Figure 2. Crystal structure of $Li_{1-x}Sn_{2+x}As_2$: (a) side view; (b) coordination of Li/Sn(1) atoms located between the As layers; (c) coordination of Sn(2) atoms surrounded by 3 As + 3 Sn(2); (d) coordination of As atoms surrounded by 3 Sn(2) and 3 Li/Sn(1) atoms; and (e) Sn−As layer showing the puckered hexagonal network. Color code: gray, Sn(2); blue, As; red, Li/Sn(1). Solid black line denotes the unit cell.

DOI: 10.1021/jacs.5b00237
J. Am. Chem. Soc. 2015, 137, 3622−3630

(Figure 1d).[26] In the case of $NaSn_2As_2$, Na atoms fully occupy the 3*a* position, which is shared among Li and Sn atoms in the case of $Li_{1-x}Sn_{2+x}As_2$.

In the crystal structure of $Li_{1-x}Sn_{2+x}As_2$, there are two Sn positions: Sn(1) in the 3*a* position, coordinated by 6 As; and Sn(2) in the 6*c* position, coordinated by 3 As + 3 Sn(2) atoms (Figure 2b,c). Arsenic atoms occupy a single position (6*c*) and are coordinated by three Sn(2) atoms and three Li/Sn(1) atoms (Figure 2d). The Sn(2) and As atoms in $Li_{1-x}Sn_{2+x}As_2$ form a network of puckered hexagons in a chair conformation (Figure 2a,e). The Li/Sn(1) atoms in the 3*a* position are located above the center of each Sn_3As_3 ring (Figure 2). The unit cell volume decreases with increasing Li content (Figure S1, left) due to shrinkage in the *ab*-plane, while the interlayer distance and unit cell parameter *c* increases. This is due to anisotropic bond distance changes. In $Li_{0.8}Sn_{2.2}As_2$, the As−Sn(2) bonds, as well as the As−Li/Sn(1) bonds, are shorter by approximately 0.02 Å compared to $Li_{0.6}Sn_{2.4}As_2$. In turn, the Sn(2)−Sn(2) bonds elongate by 0.02 Å upon increasing the Li content from 0.6 to 0.8 (Table S3).

While Sn is most often found in a tetrahedral coordination, the puckered hexagonal network is also found in KSnAs.[16] The Sn(2)−As bond distance in $Li_{1-x}Sn_{2+x}As_2$ varies from 2.70 to 2.72 Å depending on the Li content. This distance is similar to the Sn−As distance found in KSnAs (2.71−2.72 Å) and in $NaSn_2As_2$ (2.70 Å), but smaller than the Sn−As distances found in Sn_4As_3 (2.74−3.03 Å).[17] Sn−As bond distances in $SnAs_4$ tetrahedra are typically smaller in the range of 2.55−2.66 Å. Li is most often found in a tetrahedral or distorted tetrahedral coordination in Li−As compounds. Typical bond lengths are between 2.66 and 2.87 Å for Li-T-As compounds, (T = Fe, Co, Cu, Zn).[18−21]

Compounds containing both Li and Sn are found in mixed alkali metal or alkaline earth stannides.[22−24] However, only a few instances of Li/Sn substitution are found in lithium transition metal stannides: $Li_xIr_3Sn_{7-x}$, $Li_xRh_3Sn_{7-x}$, $Li_{1+x}Pd_2Sn_{6-x}$, $Li_{3-x}Pt_2Sn_{3+x}$, and $Li_{1+x}Pd_2Sn_{6-x}$.[27,28]

According to the Zintl electron count, three-coordinated Sn and As atoms tend to fulfill an electron octet by forming three covalent bonds and one electron lone pair. This requires five electrons per atom. Thus, the anionic tin−arsenic layer is negatively charged, $[Sn_2As_2]^{2-}$. Using the ionic approach, assuming a +2 oxidation state for Sn and a −3 oxidation state for As, results in the same charge for the layer, $(Sn^{2+})_2(As^{3-})_2$. Formation of an electron-balanced compound requires a +2 charge for the cation. This is realized in the isostructural compound $SrSn_2As_2$[29] and the non-isostructural compounds, NaSnP[30] and KSnAs,[16] where each Sn−P(As) layer is balanced by a layer of monovalent sodium or potassium cations. In turn, $LiSn_2As_2$ and $NaSn_2As_2$ are not electron-balanced compounds. $Li_{1-x}Sn_{2+x}As_2$ is not electron balanced for all compositions with $x < 1$ assuming that interstitial tin atoms are Sn^{2+}. Electron balance can be achieved if interstitial tin atoms have a +4 oxidation state; a compound with the composition $(Li^{1+})_{0.67}(Sn^{4+})_{0.33}[Sn_2As_2]^{2-}$ would be electron-balanced. To check the oxidation state of the tin atoms ^{119}Sn Mössbauer spectroscopy was applied.

Mössbauer Spectroscopy. Figure S2 shows the ^{119}Sn Mössbauer spectra of samples $Li_{0.73}Sn_{2.27}As_2$ and $Li_{0.8}Sn_{2.2}As_2$ at room temperature together with transmission integral fits. The corresponding fitting parameters are listed in Table S4. The spectra were successfully fitted using the results of single-crystal structure refinements. Based on the different site symmetries one can assume that the Sn(2) atoms in the 6*c* site with 3*m* local symmetry will show quadrupole splitting (3+3 coordination), while the octahedrally coordinated Sn(1) atoms in the more symmetrical 3*a* position with local site symmetry *m*3*m* will exhibit no quadrupole splitting. Fixing the tin ratios at the values obtained from the single-crystal data led to the parameters in Table S4. Both samples show very similar values for the isomer shift, the electric quadrupole splitting parameter, and experimental line widths. The spectrum of the $Li_{0.8}Sn_{2.2}As_2$ sample shows a trace impurity (~3%) of a tetravalent tin species, most probably SnO_2.

The isomer shift values of $Li_{0.73}Sn_{2.27}As_2$ and $Li_{0.8}Sn_{2.2}As_2$, 2.48−2.57 mm/s, are smaller than those recently reported for the two kinds of tin atoms in Sn_4As_3, i.e., 2.68 and 2.71 mm/s,[17] indicative of a slightly higher *s*-electron density for tin atoms in the binary arsenide. The expected isomer shift for Sn^{4+} (~0 mm/s) is quite different from the observed values. These isomer shift values are close to the one observed in the *β*-Sn modification (δ = 2.6 mm/s),[31] reflecting the metallic character of Sn. Similar values have been observed for the tin-rich lithium-stannides[32] and other intermetallic tin compounds.[33] Based on the results of Mössbauer spectroscopy we ruled out the possibility of interstitial Sn(1) atoms being in a +4 oxidation state. Thus, $Li_{1-x}Sn_{2+x}As_2$ is expected to exhibit metallic properties, which was confirmed with magnetic and resistivity measurements as well as with theoretical calculations.

Homogeneity Range and Stability. The homogeneity range of $Li_{1-x}Sn_{2+x}As_2$ was studied through X-ray diffraction (Figure S1). Single-phase samples were produced when synthesized from starting compositions such that $0.2 \leq x \leq 0.4$ with a slight excess of Li. Admixtures were produced when the starting ratios were outside of the stoichiometry range. Samples with the nominal composition in the range of $Li_{0.8}Sn_{2.2}As_2$−$Li_1Sn_2As_2$ produced compounds with a Li content not exceeding 0.8. Samples synthesized with the nominal compositions such that $x > 0.4$ produced mixtures of $Li_{0.6}Sn_{2.4}As_2$ and Sn_4As_3. The Sn and As content in the synthesized phases was additionally confirmed by EDXS analysis (Table S5).

Powder X-ray diffraction patterns of compounds with varying Li content showed broad peak widths. Analyses of various single crystals showed that while the *a* parameter decreases and the *c* parameter increases with increasing Li content, the overall unit cell volume decreases (Figure S1, left). This dependence rules out the possibility of Li intercalation into the interlayer space in between the Sn layers. Upon intercalation the unit cell volume as well as parameter *c* would increase with increasing Li content.

The compounds were stable in air for several months, but slowly decomposed after an extended time. $Li_{1-x}Sn_{2+x}As_2$ is stable upon heating to approximately 423 K in air. DSC experiments carried out in evacuated and sealed silica tubes showed that the melting points are similar for phases with different Li content (Figure S4). The peak melting and crystallization temperatures were 872(2) and 857(2) K, respectively.

Long-Range Ordering. Li and Sn atoms, which occupy the same crystallographic position, 3*a*, are quite different from a chemical bonding point-of-view, thus an ordering of Li and Sn atoms is expected. However, single-crystal and conventional powder X-ray diffraction revealed no such ordering. High-resolution synchrotron powder X-ray diffraction is much more sensitive to weak long-range ordering. We investigated two

DOI: 10.1021/jacs.5b00237
J. Am. Chem. Soc. 2015, 137, 3622−3630

samples $Li_{0.65}Sn_{2.35}As_2$ and $Li_{0.8}Sn_{2.2}As_2$ (Figure S3). For $Li_{0.8}Sn_{2.2}As_2$, all peaks present were indexed within the $R\bar{3}m$ space group using the unit cell parameters obtained from refinement of single-crystal data. In general, the structural model obtained from Rietveld refinement agrees with the single-crystal structural model. Li has a small X-ray scattering factor, but a substantial neutron scattering factor. Time-of-flight neutron powder diffraction experiments also reveal no evidence of long-range ordering or the formation of any kind of superstructure (Figure S7). Thus, the long-range ordering of Sn and Li atoms can be ruled out. However, the peaks in the high-resolution synchrotron X-ray powder pattern were quite broad and asymmetric (Figure S3, inset). This indicates possible short-range ordering in the investigated samples. Careful inspection of the synchrotron X-ray and neutron powder diffraction patterns reveal no diffraction peaks in the vicinity of 11.67 or 3.2 Å, as would be expected if the sample had admixtures of Sn_4As_3 or SnAs, respectively.

^{7}Li and ^{6}Li MAS NMR and ^{6}Li{^{7}Li} SEDOR NMR Spectroscopy. Li NMR spectroscopy has been previously used to study Li-containing compounds, in particular the electrochemical products from lithium ion battery electrodes and related Li-rich phases. Li−Sn and Li−Si phases exhibit a wide range of chemical shifts.[4,34] Furthermore, it has been previously demonstrated that cation mixing can be identified with Li NMR spectroscopy.[35] We began our short-range ordering investigation with NMR spectroscopy. The ^{7}Li and ^{6}Li MAS NMR spectra of the $Li_{1-x}Sn_{2+x}As_2$ compounds are shown in the panel on the left side in Figure 3. Each of these spectra is

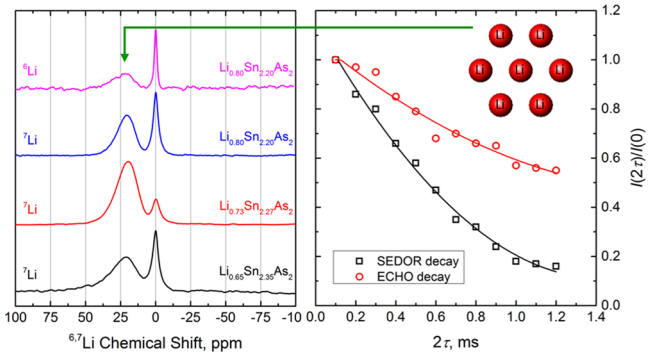

Figure 3. (Left) ^{7}Li and ^{6}Li MAS NMR spectra of $Li_{1-x}Sn_{2+x}As_2$. (Right) Normalized ^{6}Li spin echo decay (red circles) and the ^{6}Li{^{7}Li} SEDOR decay (black squares) of the broad peak in the ^{6}Li NMR spectrum for $Li_{0.8}Sn_{2.2}As_2$. Solid curve through the red circles is a second-order polynomial least-squares fit to the data. Solid curve through the black squares corresponds to a least-squares fit using the SEDOR decay equation (eq 1). Schematic of the Li environment corresponding to the broad peak near 21 ppm is shown as an overlay in the ^{6}Li spin echo plot.

characterized by a broad Gaussian peak centered at ∼21 ppm and a narrow Lorentzian peak near 0 ppm, indicating the presence of two distinct Li environments in each sample. The relative fractions of these two Li environments are clearly different for samples with different compositions; however, no systematic dependence of the relative fraction on sample composition was observed. The systematic shifts of both peak maxima with changing Li content indicate that both peaks are from the main Li−Sn−As phase and not related to any Li_2O or LiOH amorphous admixtures. We carried out ^{6}Li{^{7}Li} SEDOR spectroscopy in order to investigate whether the Gaussian broadening of the ^{7}Li and ^{6}Li NMR signal at 21 ppm can be due to Li−Li dipolar coupling in these materials.

The panel on the right side in Figure 3 shows the normalized ^{6}Li spin echo decay $F(2\tau)/F(0)$ and the ^{6}Li{^{7}Li} SEDOR decay $I(2\tau)/I(0)$ for this signal in the compound $Li_{0.8}Sn_{2.2}As_2$. The ^{6}Li spin echo decay $F(2\tau)/F(0)$ without the ^{7}Li π-pulses was fitted to a polynomial function $f(2\tau)$, and it is assumed to contribute to the SEDOR decay $I(2\tau)/I(0)$ the same way when the ^{7}Li π-pulses are present. In this scenario, the faster decay of $I(2\tau)/I(0)$ compared to that of $F(2\tau)/F(0)$ can be ascribed entirely to the dephasing of the ^{6}Li spins due to ^{6}Li−^{7}Li heteronuclear dipolar coupling.[36] If the multispin heteronuclear dipolar coupling in these compounds is characterized by a second moment M_2^{Het}, then a Gaussian decay of $I(2\tau)/I(0)$ is expected, such that

$$\frac{I(2\tau)}{I(0)} = f(2\tau)\exp\left[-\frac{(M_2^{Het})^2}{2}\right] \quad (1)$$

This equation was used to fit the experimental $I(2\tau)/I(0)$ data in Figure 3, which yielded a M_2^{Het} value of 2.4×10^6 rad^2/s^2. For the calculated M_2^{Het} value we considered an ideal structure of $LiSn_2As_2$ where each Li atom is surrounded by six neighboring Li atoms at a distance of ∼4 Å distance within the [001] plane. The calculated M_2^{Het} value, 2.5×10^6 rad^2/s^2, is in good agreement with the experimental value. The calculated M_2^{Het} is given by the van Vleck relation,[37]

$$M_2^{Het} = \frac{4}{15}\left(\frac{\mu_0}{4\pi}\right)^2 \gamma_I^2 \gamma_S^2 \hbar^2 S(S+1) \sum_n r_{IS}^{-6} \quad (2)$$

In this equation, r_{IS} is the distance between a central ^{6}Li and its nearest neighbor ^{7}Li nuclides and the summation is for all ^{6}Li−^{7}Li pairs, i.e., $n = 6$; γ_I and γ_S are the gyromagnetic ratios of ^{6}Li and ^{7}Li nuclides, and $S = 3/2$ is the nuclear spin quantum number for ^{7}Li. The natural abundance of the two Li isotopes was taken into account in our calculation of M_2^{Het}. Therefore, the broad Gaussian peak at ∼21 ppm in the ^{6}Li and ^{7}Li MAS NMR spectra can be assigned to a Li atom surrounded by six other Li atoms in the structure of $LiSn_2As_2$. The peak broadening of this component is dominated by Li−Li dipolar interaction and not by any structural inhomogeneities. Thus, solid-state NMR spectroscopy clearly indicates that local segregation of Li and Sn takes place and that part of the sample has the ideal composition, $LiSn_2As_2$.

The narrow peak in the ^{6}Li and ^{7}Li MAS NMR spectra at ∼0 ppm corresponds to structurally "isolated" Li atoms, i.e., Li atoms without a significant number of Li neighbors. These assignments are consistent with the TEM results (*vide infra*) that indicate that $Li_{1-x}Sn_{2+x}As_2$ segregates locally to $LiSn_2As_2$ and Li−Sn_4As_3 or Li-SnAs phases with low Li content. Hence, the two peaks at 21 and 0 ppm in the ^{6}Li and ^{7}Li MAS NMR can be assigned to Li sites in the Li-rich and Sn-rich phases, respectively.

Transmission Electron Microscopy (TEM). TEM studies show that the structure is perfectly ordered at the nanoscale. However, the material consists of numerous defects and intergrowths. Multiple anti-phase boundary (APB) defects were revealed by HRTEM investigation of the main phase $Li_{1-x}Sn_{2+x}As$, probably due to non-uniform Li/Sn distribution. Figure S5 shows APBs viewed along two most informative zone axes, [100] (Figure S5a) and [120] (Figure S5b) where the shift of the respective planes along the *c*-axis is clearly visible.

DOI: 10.1021/jacs.5b00237
J. Am. Chem. Soc. 2015, 137, 3622−3630

The electron diffraction patterns are in agreement with the average structural model. The [00*l*] reflection from powder XRD has a very broad and asymmetric shape. In electron diffraction some incommensurability for the [00*l*] diffraction peaks was also observed (Figure S5, inset).

Careful investigations of the samples reveal the presence of areas that are distinct from the main phase. In these areas, an intergrowth of two binary arsenides, SnAs and Sn_4As_3, was observed (Figures 4 and S6). Figure 4 shows a set of ED

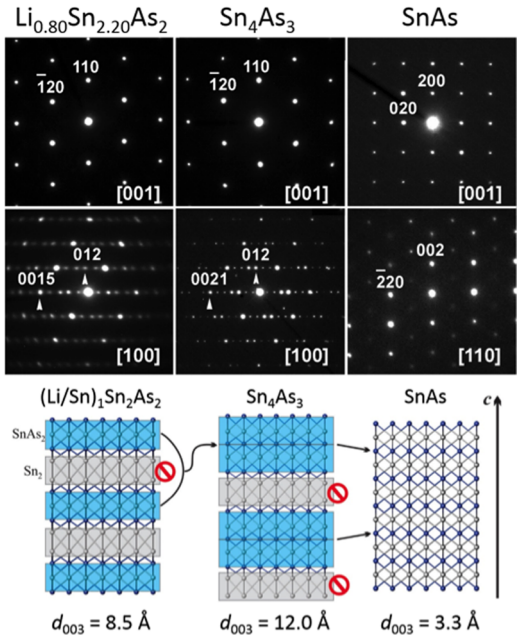

Figure 4. (Top) Observed ED patterns of $Li_{1-x}Sn_{2+x}As_2$, Sn_4As_3, and SnAs from a single sample of $Li_{0.80}Sn_{2.20}As_2$. (Bottom) Model of the structural transformation from $LiSn_2As_2$ to Sn_4As_3 to SnAs. Note that [111] for cubic SnAs is analogous to [001] for both $LiSn_2As_2$ and Sn_4As_3.

patterns of the main zones for all phases and corresponding structural models. Cubic SnAs crystallizes in a NaCl type F-cubic structure.[38] When SnAs is considered in a rhombohedral setting, SnAs and Sn_4As_3 have the *a* unit cell parameters of 4.02 and 4.09 Å at room temperature, respectively, that are very similar to the *a* parameter in $Li_{1-x}Sn_{2+x}As_2$, 4.02−3.99 Å at 90 K. Thus, the [001] direction for Sn_4As_3 and [111] direction for SnAs are nearly indistinguishable in the electron diffraction patterns. The similar hexagonal bases allow for the possibility of intergrowths. The structural relationships among the three Sn−As phases and the different stacking of Sn−As and Sn−Sn layers are shown in the bottom of Figure 4.

Significant shortening of the *c* unit cell parameter was detected for both binary Sn−As phases. Thus, the observed Sn−As phases are not true binary phases but probably contain a certain amount of Li. For binary bulk phases, d_{003} of 12.0 Å and d_{111} of 3.3 Å are expected for Sn_4As_3 and SnAs, respectively. The corresponding distances calculated from the experimental electron diffraction patterns in Figure 4 are 11.67 and 3.2 Å for Sn_4As_3 and SnAs, respectively, which indicates that there is significant shortening along the direction of the stacked layers in these phases, presumably due to Li/Sn substitutions. These data agree with the results of NMR spectroscopy indicating that phases with effectively isolated Li atoms are present in the sample. TEM data indicates that Li atoms are effectively isolated from each other in the structures of the "SnAs" and "Sn_4As_3" pseudo-binary phases.

HAADF-STEM provides additional clues regarding the intergrowths and in particular provides information about the SnAs and Sn_4As_3 binary phases (Figure 5). Two dark rows were

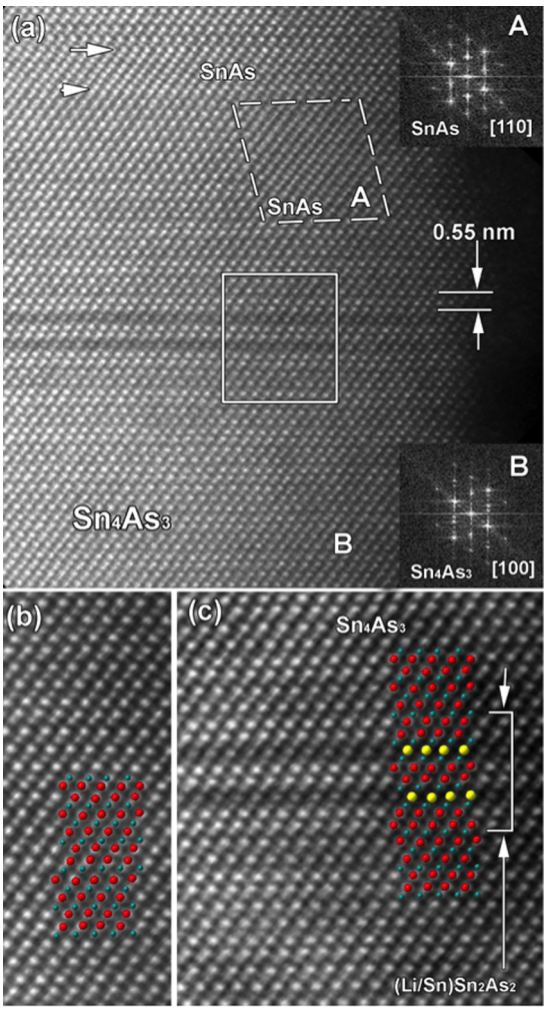

Figure 5. (a) HAADF-STEM image of the intergrowth boundary between SnAs (A) and Sn_4As_3 (B). Corresponding FT patterns are shown as insets. Below are shown enlarged portions of the HAADF-STEM image of (b) the pristine Sn_4As_3 image and (c) the interface showing two rows of Li atoms overlapped with corresponding structural models. Color code: red, Sn; cyan, As; yellow, Li/Sn.

clearly observed in the HAADF-STEM image, which correspond to Li-rich atomic columns (Figure 5). Such contrast changes was observed in oxide systems and was attributed to increasing distances between successive cationic layers due to the non-stoichiometry of oxygen atoms.[39] In our case, such contrast in the HAADF-STEM image can be explained by increasing the distance between successive Sn/As layers due to Li insertion. A structural model is shown in Figure 5. This model corresponds to the aforementioned formation of $LiSn_2As_2$ from Sn_4As_3 by substitution of rows of Sn atoms for Li atoms (Figure 1).

TEM investigations showed that $Li_{1-x}Sn_{2+x}As_2$ exhibits non-uniform local distribution of Li and Sn atoms with multiple defects. Segregation of $Li_{1-x}Sn_{2+x}As_2$ into Li-rich areas with the $LiSn_2As_2$ structure and Li-poor areas with SnAs and Sn_4As_3

DOI: 10.1021/jacs.5b00237
J. Am. Chem. Soc. 2015, 137, 3622−3630

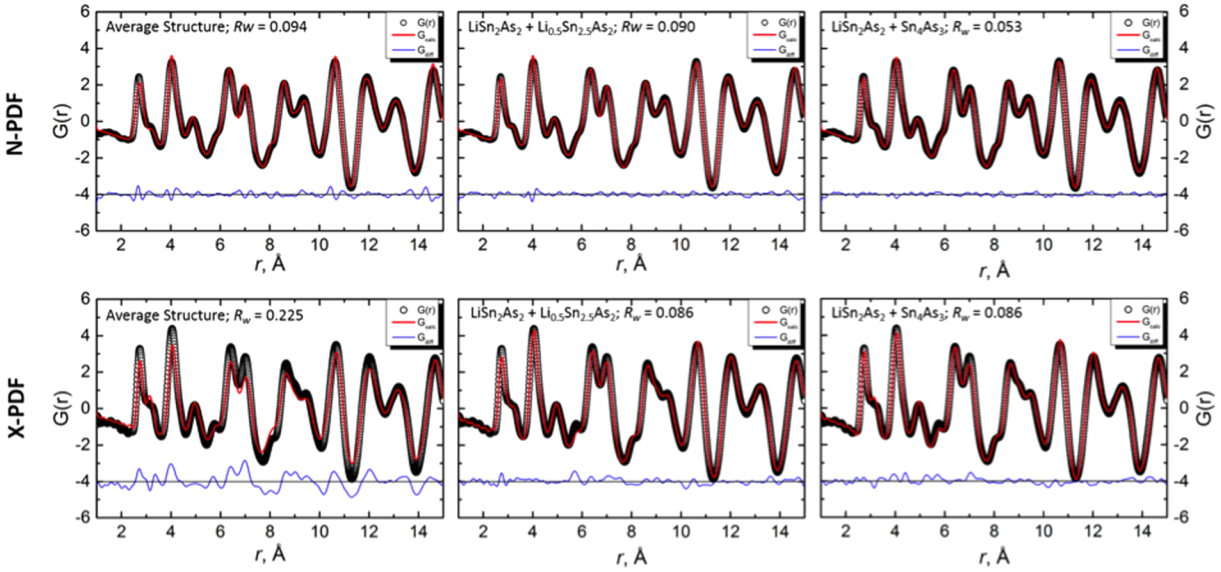

Figure 6. Short-range (r = 1−15 Å) pair distribution function plots for $Li_{0.65}Sn_{2.35}As_2$. (Top) Neutron PDF (N-PDF) and (bottom) X-ray PDF (X-PDF) plots for three different models: average structure model (left); two-phase model with $LiSn_2As_2$ and $Li_{0.5}Sn_{2.5}As_2$ (center); and two-phase model with $LiSn_2As_2$ and Sn_4As_3 (right).

structures were observed through TEM and are in agreement with the results of the NMR spectroscopic investigations. No evidence of diffraction peaks near 11.67 and 3.2 Å was found in the high-resolution synchrotron powder X-ray diffraction pattern, strongly suggesting that the formation of the pseudo-binary phases, SnAs and Sn_4As_3, occurs only on the local scale.

Pair Distribution Function (PDF). It has been previously demonstrated that atomic pair distribution analysis can be used to characterize materials with disorder and provide information about long- and short-range ordering.[40−42] Rietveld refinement of neutron powder diffraction data was used to obtain an average model, which became the starting model for the neutron-PDF (N-PDF) refinement. The refined unit cell parameters and the average Li/Sn ratios match those values obtained from single-crystal experiments. Refinement of N-PDF with the single-crystal structural model with the 3*a* position jointly occupied by Li and Sn atoms fits relatively well at short range, r = 1−15 Å, though the broad peak at ∼2.7 Å is not satisfactorily described (Figure 6). This peak is a superposition of the Li/Sn(1)−As and the Sn(2)−As interatomic distances. In addition, the refined Li content was much lower than what was calculated from the single-crystal model. NMR spectroscopy shows that Li segregates into regions of different Li environments: Li atoms surrounded by six other Li atoms within the layer, and Li atoms in a more Sn-rich environment. The next stage of the refinement was performed with two phases, $LiSn_2As_2$ and $Li_{0.5}Sn_{2.5}As_2$, corresponding to two different Li contents as suggested by NMR spectroscopy. The unit cells and atomic coordinates for the two different phases were allowed to refine while applying crystallographic constraints, and fixing the ratio of the phases to generate the average composition close to the one determined by single-crystal and powder neutron diffraction, $Li_{0.65}Sn_{2.35}As_2$. The addition of the second phase resulted in a much better fit of the peak at ∼2.76 Å. Refined unit cell parameters were consistent with the trend observed in single-crystal analysis. The $LiSn_2As_2$ phase has a smaller unit cell volume and *a* parameter in comparison to $Li_{0.5}Sn_{2.5}As_2$. Moreover, the refined unit cell volume for $LiSn_2As_2$ is smaller than the volume of any compound reported in Table S1. The Li−As and Sn−As interatomic distances are also consistent with the trends observed for average structure.

TEM investigations suggest that instead of the tin-rich $Li_{0.5}Sn_{2.5}As_2$ phase, other pseudo-binary Li-containing phases "SnAs" and "Sn_4As_3" are formed. N-PDF data were fitted with an additional model: $LiSn_2As_2$ + Sn_4As_3, which gave the best fit in the small r region with the smoothest difference curve, especially for the first peak at ∼2.76 Å (Figure 6, top). Similar results were obtained when $LiSn_2As_2$ + SnAs mixture was refined (Figure S8). Refinement of a three-phase mixture was not performed to avoid over parameterization.

The X-ray PDF (X-PDF) cannot be satisfactorily described with the average structural model. Two-phase fitting, similar to N-PDF, resulted in good agreement between the experimental and calculated PDF patterns (Figure 6, bottom). While both the average structure model and two-phase model gave similar fits for N-PDF data, the disparity between the two models was much more apparent in the refinement of X-PDF data. Refinements of the two-phase mixtures of $LiSn_2As_2$ and either Sn_4As_3 or SnAs also provided a better fit of the experimental X-PDF data compared to the average model. In general, the fitted structural parameters are similar for N- and X-PDF.

Refinements of small r ranges with the two-phase model resulted in better fits, suggesting the presence of local domains. At larger r ranges, the structure should be similar to the average phase determined from single-crystal data. However, refinement of X-PDF and N-PDF at larger r-values did not result in a significantly better fit when the average structure model was used instead of the two-phase model. This suggests that the nanoinclusions were of substantial size, several nanometers rather than one unit cell, which is in agreement with observations from TEM. PDF data strongly supports the local segregation of Li and Sn atoms into two phases with significantly different Li content and unit cell parameters.

Electronic Structure Calculations. Band structure calculations were performed on four different models with varying Li content. The density of states (DOS) and band structures were calculated for four different models (A−D) with varying Li

DOI: 10.1021/jacs.5b00237
J. Am. Chem. Soc. 2015, 137, 3622−3630

content. Details pertaining to the band structure calculations are found in the SI. All calculated models predicted $Li_{1-x}Sn_{2+x}As_2$ to be metallic with a pronounced pseudo-gap. The band structure of all $Li_{1-x}Sn_{2+x}As_2$ models showed large anisotropy across different crystallographic directions. In particular, in the band structure of model $Li_{0.67}Sn_{2.33}As_2$, there are no bands that cross the Fermi level in the Γ-A, K-M, and L-H directions (Figure S10). For compounds with a higher Li content, we expected the Fermi level would shift down when decreasing the total number of electrons. Indeed, the band structure of $Li_{0.83}Sn_{2.17}As_2$ is similar to the band structure of $Li_{0.67}Sn_{2.33}As_2$, but with the Fermi level now crossing bands across all directions. From the band structures of these models, highly anisotropic electronic behavior was expected. In addition, compounds with a higher Li content were expected to be more conductive than compounds with a lower Li content.

ELF analysis was performed on a model with the composition $Li_{0.67}Sn_{2.33}As_2$. ELF analysis confirmed the expected covalent bond (attractors ② and ③) between the Sn(2) and As atoms with the lone pair electrons of Sn(2) directed toward the Sn(2)−Sn(2) interlayer space (attractor ①) similar to the Sn atoms in the structure of Sn_4As_3 (Figure 7).[17]

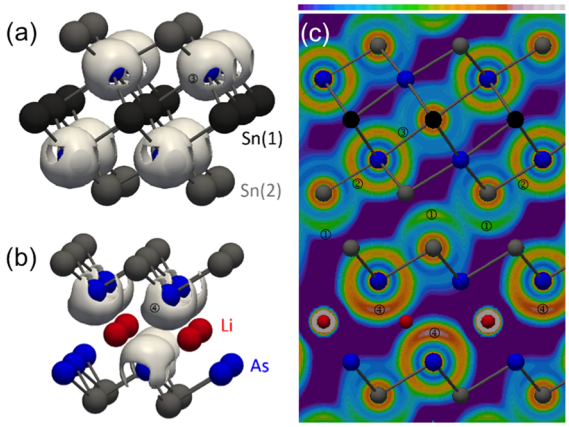

Figure 7. ELF isosurfaces and slice of $Li_{0.67}Sn_{2.33}As_2$: (a) isosurface depicting the Sn(1)−As and Sn(2)−As bonds, η = 0.624; (b) lone pair electrons on As atoms directed toward Li, η = 0.72; and (c) [110] slice. The scale is given on the top of panel (c).

Significant differences were seen between the As−Li and As−Sn(1) bonding. The As atoms for the Li−As layer exhibit a lone pair directed toward the Li atoms (attractor ④) and deep ELF minima surrounding the Li atoms (Figures 7C and S11D,E). The ELF around the As atoms in the Sn(1)−As layers is less structured. There are no deep ELF minima around Sn(1) atoms, instead a weak maxima ③ is observed. Figure S11 shows slices through the Sn(1) layer and a slice above the Sn(1) layer closer to the As. These slices show that there is no deep minimum surrounding the Sn(1) atoms as in the case of Li. ELF analysis suggests the presence of multicenter bonding between As and three Sn(1) atoms. The presence of Sn atoms surrounded by a regular As_6 octahedron was recently proposed to be a reason for unconventional superconductivity in SnAs, where a +3 oxidation state was assumed.[43] The bond valence sum calculations for $Li_{0.67}Sn_{2.33}As_2$ result in a similar value of +3.0 for Sn(1) surrounded by As octahedron. The bond valence sum calculations for Li in the same crystallograhic position result in a significantly smaller charge of +0.8 which is close to the expected +1 oxidation state for Li.[44] Crystal orbital Hamilton population (COHP) calculations were also performed for the model used for ELF analysis. Integrated COHP values of Li−As, Sn(1)−As, and Sn(2)−Sn(2) were found to be 0.35, 1.43, and 1.65, respectively, indicating that there is a much stronger bonding interaction for the Sn(1) atoms than the Li atoms in the As octahedra. Similar bonding studies were performed for $SrAs_2Sn_2$, which showed a small overlap population for the Sr−As interaction and a much larger overlap population for the Sn−Sn interactions, which is consistent with the results of our ELF and COHP calculations.[45] Our calculations reveal a strong difference in the chemical bonding for Sn and Li atoms occupying the same crystallographic position. We hypothesize that this difference is the driving force for the observed short-range ordering.

Magnetic and Transport Properties. In agreement with the theoretical calculations, all studied compounds exhibited temperature independent Pauli paramagnetism in the studied range of 50−300 K. Calculations predict a higher density of states at the Fermi level for Li-rich compositions, which agree with the experimental magnetic susceptibilities: 2.6×10^{-5} and 4.1×10^{-5} emu/mol for $Li_{0.74}Sn_{2.26}As_2$ and $Li_{0.65}Sn_{2.35}As_2$, respectively (Figure S13).

The measured Seebeck thermopower for all $Li_{1-x}Sn_{2+x}As_2$ compositions is positive, indicating that holes are the main charge carriers. At room temperature, the values of the thermopower do not exceed +10 μV/K. As expected from band structure calculations, all $Li_{1-x}Sn_{2+x}As_2$ compositions exhibit metallic-type resistivity. The resistivity was strongly anisotropic with higher resistivity perpendicular to the Sn_2As_2 layers (Figure 8, left). According to calculations, while a higher

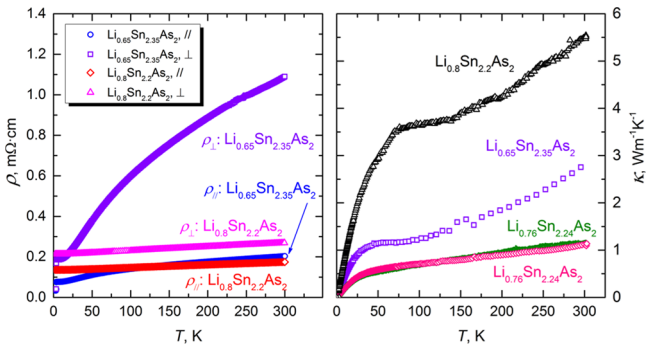

Figure 8. (Left) Resistivity of $Li_{0.65}Sn_{2.35}As_2$ and $Li_{0.78}Sn_{2.22}As_2$ parallel and perpendicular to the layers. (Right) Thermal conductivity of four different crystals of $Li_{1-x}Sn_{2+x}As_2$.

out-of-plane resistivity is expected for all $Li_{1-x}Sn_{2+x}As_2$ compositions, this effect should be more pronounced for the Li-poor compositions (Figure S10). At room temperature, the $\rho_\perp/\rho_\parallel$ ratio is 1.5 and 5.4 for $Li_{0.78}Sn_{2.22}As_2$ and $Li_{0.65}Sn_{2.35}As_2$, respectively, which is in good agreement with the theoretical predictions.

All compositions of $Li_{1-x}Sn_{2+x}As_2$ exhibit unexpectedly low thermal conductivity in the range of 1−6 W m^{-1} K^{-1} at 300 K. For each sample, several crystals were measured with typical examples shown in Figure 8 (right). The densities of the crystals were >95% of the X-ray density and crystals were cleaved with Scotch tape to remove possible oxides from the surface. Thermal conductivity was measured in the direction perpendicular to the Sn_2As_2 layers. The thermal conductivity slightly depends on the thickness of the measured crystal with a

DOI: 10.1021/jacs.5b00237
J. Am. Chem. Soc. 2015, 137, 3622−3630

general tendency that thinner crystals exhibit lower thermal conductivity.

$Li_{0.8}Sn_{2.2}As_2$ and $Li_{0.65}Sn_{2.35}As_2$ exhibit a peak in thermal conductivity at 50−75 K, which is typical for crystalline compounds. For $Li_{0.76}Sn_{2.24}As_2$ no such peak was detected, which is typical for amorphous or strongly disordered solids. The high temperature increase in thermal conductivity is probably due to the radiative losses. The difference in the thermal conductivity between $Li_{0.8}Sn_{2.2}As_2$ and $Li_{0.65}Sn_{2.35}As_2$ cannot be explained simply by different charge carrier contributions. At 100 K the highest possible values of the electronic contribution to thermal conductivity were estimated to be 1.1 ($Li_{0.8}Sn_{2.2}As_2$) and 0.4 W m^{-1} K^{-1} ($Li_{0.65}Sn_{2.35}As_2$), using $\rho_\perp$, the Wiedemann−Franz law, and $(1/3)(\pi k_B/e)^2$ as the Lorenz number. This indicates that the lattice contribution to the thermal conductivity is ∼3 times higher for $Li_{0.8}Sn_{2.2}As_2$ compared to $Li_{0.65}Sn_{2.35}As_2$. Moreover, there is no direct correlation between the value of thermal conductivity and the Li content in $Li_{1-x}Sn_{2+x}As_2$, in line with the observations from NMR spectroscopy that the Li-rich/Li-poor phase ratio is not proportional to the Li content. Several crystals from the sample with $x = 0.76$ were measured and the resulting curves lie on top of each other, two of them are shown in red and blue in Figure 8. Compounds with decoupled electron and phonon transport fulfill the requirements of the phonon glass−electron crystal (PGEC) concept, and is expected to exhibit high values of $1/\rho\kappa$. For the $Li_{1-x}Sn_{2+x}As_2$ sample with $x = 0.76$, the calculated value of $1/\rho\kappa$ at room temperature is as high as 350×10^3 K Ω^{-1} W^{-1}, which situates this compound among the best PGEC materials.[46]

Low thermal conductivity is found in compounds with large unit cells and complex structures,[47] e.g., $Ba_8Au_{16}P_{30}$[13] and $Gd_{117}Co_{56}Sn_{112}$.[46] Though the unit cell of $Li_{1-x}Sn_{2+x}As_2$ is comparatively small and simple with only three crystallographic positions, $Li_{1-x}Sn_{2+x}As_2$ displays low thermal conductivity. The mechanism for low thermal conductivity is attributed to presence of nanosized domains of Sn_4As_3 and SnAs that were detected by NMR spectroscopy, PDF, and TEM. Nanoinclusions and phase boundaries have been reported to effectively reduce the thermal conductivity. Nanostructured modifications of various chalcogenides, such as PbTe or Bi_2Te_3, have demonstrated the effectiveness of composite materials or nanoscale structural engineering to reduce thermal conductivity.[48−52] Multiple twinning and antiphase boundaries in the $Ba_8Au_{16}P_{30}$ clathrate also led to a reduction of lattice thermal conductivity.[13] In $Li_{1-x}Sn_{2+x}As_2$, nanoscale ordering and the presence of small domains with different chemical compositions and different unit cells result in the formation of natural superstructures that scatter heat-carrying phonons. The mechanism of creating local inhomogeneities by mixing two cations of very different chemical nature in one position may be used for the development of novel thermoelectric materials.

CONCLUSIONS

A new ternary lithium tin arsenide, $Li_{1-x}Sn_{2+x}As_2$, was synthesized via solid-state synthesis from elements. $Li_{1-x}Sn_{2+x}As_2$ exhibits local ordering of Li/Sn atoms that was investigated by HRTEM, STEM, solid-state ^{6,7}Li SEDOR NMR spectroscopy, and PDF analysis. NMR spectroscopy suggests the presence of two types of Li atoms within the compound. Coupled NMR experiments show that one type of Li atom is situated in a Li-rich environment with six Li neighbors, while the second type of Li atom is essentially isolated. HRTEM and PDF analyses indicated that $Li_{1-x}Sn_{2+x}As_2$ segregated into Li-rich ($LiSn_2As_2$) and Sn-rich (Sn_4As_3- and SnAs-like) nanoscale domains. Electronic structure investigations predict anisotropic metallic properties. ELF analysis indicates the presence of covalent 2c-2e and multicenter Sn−As bonds. $Li_{1-x}Sn_{2+x}As_2$ exhibits highly anisotropic metallic resistivity. The presence of local ordering of Li/Sn atoms leads to the unexpectedly low thermal conductivity for this metallic, crystalline compound.

ASSOCIATED CONTENT

Supporting Information

Experimental details, tables of crystal structure refinements and structural parameters and associated CIF files, ^{119}Sn Mössbauer spectra and fitting parameters, energy-dispersive X-ray spectroscopy results, differential scanning calorimetry plots, synchrotron X-ray and neutron powder diffraction Rietveld refinement plots, N-PDF and X-PDF of the $LiSn_2As_2$ + SnAs structural model, additional TEM figures, details of the electronic structure calculations, DOS and band structure diagrams for different models of $Li_{1-x}Sn_{2+x}As_2$, as well as for Sn_4As_3, Sn_3As_2, and $NaSn_2As_2$, additional ELF figure for $Li_{0.67}Sn_{2.33}As_2$, and magnetic susceptibility data. This material is available free of charge via the Internet at http://pubs.acs.org.

AUTHOR INFORMATION

Corresponding Author

*kkovnir@ucdavis.edu

Notes

The authors declare no competing financial interest.

ACKNOWLEDGMENTS

This research is supported by the U.S. Department of Energy, Office of Basic Energy Sciences, Division of Materials Sciences and Engineering, under Award No. DE-SC0008931. Use of the Advanced Photon Source at Argonne National Laboratory was supported by the U.S. Department of Energy, Office of Science, Office of Basic Energy Sciences, under Contract No. DE-AC02-06CH11357. Research conducted at ORNL's Spallation Neutron Source was sponsored by the Scientific User Facilities Division, Office of Basic Energy Sciences, U.S. Department of Energy. The National High Magnetic Field Laboratory is supported through the National Science Foundation Cooperative Agreement (DMR-0084173) and by the State of Florida. We thank Prof. S. M. Kauzlarich for access to the DSC. K.L. acknowledges the GAANN fellowship.

REFERENCES

(1) Kamaya, N.; Homma, K.; Yamakawa, Y.; Hirayama, M.; Kanno, R.; Yonemura, M.; Kamiyama, T.; Kato, Y.; Hama, S.; Kawamoto, K.; Mitsui, A. *Nat. Mater.* **2011**, *10*, 682.
(2) Goodenough, J. B.; Park, K.-S. *J. Am. Chem. Soc.* **2013**, *135*, 1167.
(3) Mo, Y.; Ong, S. P.; Ceder, G. *Chem. Mater.* **2011**, *24*, 15.
(4) Key, B.; Morcrette, M.; Tarascon, J.-M.; Grey, C. P. *J. Am. Chem. Soc.* **2010**, *133*, 503.
(5) Zeilinger, M.; Kurylyshyn, I. M.; Häussermann, U.; Fässler, T. F. *Chem. Mater.* **2013**, *25*, 4623.
(6) Wang, J.; Chen-Wiegart, Y.-c. K.; Wang, J. *Angew. Chem., Int. Ed.* **2014**, *53*, 4460.
(7) Dupke, S.; Eckert, H.; Winter, F.; Pöttgen, R. *Prog. Solid State Chem.* **2014**, *42*, 57.
(8) Pöttgen, R.; Eckert, T. D.; Sreeraj, P.; Wiemhöfer, H.-D. *Z. Phys. Chem.* **2010**, *224*, 1475.
(9) Mozharivskyj, Y.; Pecharsky, A. O.; Bud'ko, S.; Miller, G. J. *Chem. Mater.* **2004**, *16*, 1580.

DOI: 10.1021/jacs.5b00237
J. Am. Chem. Soc. 2015, 137, 3622−3630

(10) Nylén, J.; Andersson, M.; Lidin, S.; Häussermann, U. *J. Am. Chem. Soc.* **2004**, *126*, 16306.
(11) Snyder, G. J.; Christensen, M.; Nishibori, E.; Caillat, T.; Iversen, B. B. *Nat. Mater.* **2004**, *3*, 458.
(12) Iversen, B. B. *J. Mater. Chem.* **2010**, *20*, 10778.
(13) Fulmer, J.; Lebedev, O. I.; Roddatis, V. V.; Kaseman, D. C.; Sen, S.; Dolyniuk, J.-A.; Lee, K.; Olenev, A. V.; Kovnir, K. *J. Am. Chem. Soc.* **2013**, *135*, 12313.
(14) Agha, E. C.; Malliakas, C. D.; Im, J.; Jin, H.; Zhao, L.-D.; Freeman, A. J.; Kanatzidis, M. G. *Inorg. Chem.* **2014**, *53*, 673.
(15) Asbrand, M.; Eisenmann, B.; Klein, J. *Z. Anorg. Allg. Chem.* **1995**, *621*, 576.
(16) Lii, K. H.; Haushalter, R. C. *J. Solid State Chem.* **1987**, *67*, 374.
(17) Kovnir, K.; Kolen'ko, Y. V.; Baranov, A. I.; Neira, I. S.; Sobolev, A. V.; Yoshimura, M.; Presniakov, I. A.; Shevelkov, A. V. *J. Solid State Chem.* **2009**, *182*, 630.
(18) Mito, M.; Pitcher, M. J.; Crichton, W.; Garbarino, G.; Baker, P. J.; Blundell, S. J.; Adamson, P.; Parker, D. R.; Clarke, S. J. *J. Am. Chem. Soc.* **2009**, *131*, 2986.
(19) Juza, R.; Langer, K. *Z. Anorg. Allg. Chem.* **1968**, *361*, 58.
(20) Benda, K. V.; Juza, R. *Z. Anorg. Allg. Chem.* **1969**, *371*, 172.
(21) Hönle, W. *Z. Naturforsch. B* **1993**, *48*, 683.
(22) Bobev, S.; Sevov, S. C. *Angew. Chem., Int. Ed.* **2001**, *40*, 982.
(23) Bobev, S.; Sevov, S. C. *J. Alloys Compd.* **2002**, *338*, 87.
(24) Wu, Z.; Mosel, B. D.; Eckert, H.; Hoffmann, R.-D.; Pöttgen, R. *Chem.—Eur. J.* **2004**, *10*, 1558.
(25) Hoffmann, R.-D.; Johrendt, D.; Wu, Z.; Pottgen, R. *J. Mater. Chem.* **2002**, *12*, 676.
(26) Wu, Z.; Eckert, H.; Senker, J.; Johrendt, D.; Kotzyba, G.; Mosel, B. D.; Trill, H.; Hoffmann, R.-D.; Pöttgen, R. *J. Phys. Chem. B* **2003**, *107*, 1943.
(27) Sreeraj, P.; Hoffmann, R.-D.; Wu, Z.; Pöttgen, R.; Häussermann, U. *Chem. Mater.* **2005**, *17*, 911.
(28) Sreeraj, P.; Kurowski, D.; Hoffmann, R.-D.; Wu, Z.; Pöttgen, R. *J. Solid State Chem.* **2005**, *178*, 3420.
(29) Eisenmann, B.; Klein, J. *Z. Anorg. Allg. Chem.* **1991**, *598*, 93.
(30) Eisenmann, B.; Rößler, U. *Z. Krist.-New Cryst. St.* **1998**, *213*, 28.
(31) Lippens, P. E. *Phys. Rev. B* **1999**, *60*, 4576.
(32) Robert, F.; Lippens, P. E.; Olivier-Fourcade, J.; Jumas, J. C.; Gillot, F.; Morcrette, M.; Tarascon, J. M. *J. Solid State Chem.* **2007**, *180*, 339.
(33) Pöttgen, R. *Z. Naturforsch.* **2006**, *61b*, 677.
(34) Bekaert, E.; Robert, F.; Lippens, P. E.; Ménétrier, M. *J. Phys. Chem. C* **2010**, *114*, 6749.
(35) Cahill, L. S.; Yin, S. C.; Samoson, A.; Heinmaa, I.; Nazar, L. F.; Goward, G. R. *Chem. Mater.* **2005**, *17*, 6560.
(36) Peter Puls, S.; Eckert, H. *Phys. Chem. Chem. Phys.* **2007**, *9*, 3992.
(37) Van Vleck, J. H. *Phys. Rev.* **1948**, *74*, 1168.
(38) Peretti, E. A.; Paulsen, J. K. *J. Less-Common Metals* **1969**, *17*, 283.
(39) Volkova, N. E.; Lebedev, O. I.; Gavrilova, L. Y.; Turner, S.; Gauquelin, N.; Seikh, M. M.; Caignaert, V.; Cherepanov, V. A.; Raveau, B.; Van Tendeloo, G. *Chem. Mater.* **2014**, *26*, 6303.
(40) Liu, B.; Abouimrane, A.; Ren, Y.; Neufeind, J.; Fang, Z. Z.; Amine, K. *J. Electrochem. Soc.* **2013**, *160*, A882.
(41) Petkov, V.; Ren, Y.; Kabekkodu, S.; Murphy, D. *Phys. Chem. Chem. Phys.* **2013**, *15*, 8544.
(42) Yamakawa, N.; Jiang, M.; Key, B.; Grey, C. P. *J. Am. Chem. Soc.* **2009**, *131*, 10525.
(43) Wang, Y.; Sato, H.; Toda, Y.; Ueda, S.; Hiramatsu, H.; Hosono, H. *Chem. Mater.* **2014**, *26*, 7209.
(44) Brese, N. E.; O'Keeffe, M. *Acta Crystallogr., Sect B: Struct. Sci.* **1991**, *B47*, 192.
(45) Alemany, P.; Llunell, M.; Canadell, E. *J. Comput. Chem.* **2008**, *29*, 2144.
(46) Schmitt, D. C.; Haldolaarachchige, N.; Xiong, Y.; Young, D. P.; Jin, R.; Chan, J. Y. *J. Am. Chem. Soc.* **2012**, *134*, 5965.
(47) Toberer, E. S.; Zevalkink, A.; Snyder, G. J. *J. Mater. Chem.* **2011**, *21*, 15843.
(48) Satyala, N.; Tahmasbi Rad, A.; Zamanipour, Z.; Norouzzadeh, P.; Krasinski, J. S.; Tayebi, L.; Vashaee, D. *J. Appl. Phys.* **2014**, *115*, No. 044304.
(49) Hori, T.; Chen, G.; Shiomi, J. *Appl. Phys. Lett.* **2014**, *104*, No. 021915.
(50) Sootsman, J. R.; Kong, H.; Uher, C.; D'Angelo, J. J.; Wu, C.-I.; Hogan, T. P.; Caillat, T.; Kanatzidis, M. G. *Angew. Chem., Int. Ed.* **2008**, *47*, 8618.
(51) Biswas, K.; He, J.; Blum, I. D.; Wu, C.-I.; Hogan, T. P.; Seidman, D. N.; Dravid, V. P.; Kanatzidis, M. G. *Nature* **2012**, *489*, 414.
(52) Poudeu, P. F. P.; D'Angelo, J.; Kong, H.; Downey, A.; Short, J. L.; Pcionek, R.; Hogan, T. P.; Uher, C.; Kanatzidis, M. G. *J. Am. Chem. Soc.* **2006**, *128*, 14347.

DOI: 10.1021/jacs.5b00237
J. Am. Chem. Soc. 2015, 137, 3622−3630